

PAPER • OPEN ACCESS

## Acousto-optic scanning spatial-switching multiphoton lithography





To cite this article: Binzhang Jiao *et al* 2023 *Int. J. Extrem. Manuf.* **5** 035008

View the [article online](#) for updates and enhancements.

### You may also like

- [Energy consumption and mechanical proprieties of Hybrid Deposition & Micro-Rolling](#)  
Cheng Huang, Haiou Zhang and Guilan Wang
- [Transformer-based radio modulation mode recognition](#)  
Lingyun Li, Chanchan Qin, Guoqing Li et al.
- [Research on damage characteristics and microscopic appearance of ReBCO tapes after DC overcurrent](#)  
Zili Yang, Ying Xu, Xianhao Li et al.

# Acousto-optic scanning spatial-switching multiphoton lithography

Binzhang Jiao<sup>1</sup> , Fayu Chen<sup>1</sup>, Yuncheng Liu<sup>1</sup>, Xuhao Fan<sup>1</sup> , Shaoqun Zeng<sup>1,2</sup>, Qi Dong<sup>1</sup>, Leimin Deng<sup>1,2</sup>, Hui Gao<sup>1,2,\*</sup>  and Wei Xiong<sup>1,2,\*</sup> 

<sup>1</sup> Wuhan National Laboratory for Optoelectronics and School of Optical and Electronic Information, Huazhong University of Science and Technology, Wuhan, Hubei 430074, People's Republic of China

<sup>2</sup> Optics Valley Laboratory, Wuhan, Hubei 430074, People's Republic of China

E-mail: [gaohui\\_wnlo@hust.edu.cn](mailto:gaohui_wnlo@hust.edu.cn) and [weixiong@hust.edu.cn](mailto:weixiong@hust.edu.cn)

Received 13 April 2023, revised 14 May 2023

Accepted for publication 21 June 2023

Published 4 July 2023



CrossMark

## Abstract

Nano-3D printing has obtained widespread attention owing to its capacity to manufacture end-use components with nano-scale features in recent years. Multiphoton lithography (MPL) is one of the most promising 3D nanomanufacturing technologies, which has been widely used in manufacturing micro-optics, photonic crystals, microfluidics, meta-surface, and mechanical metamaterials. Despite of tremendous potential of MPL in laboratorial and industrial applications, simultaneous achievement of high throughput, high accuracy, high design freedom, and a broad range of material structuring capabilities remains a long-pending challenge. To address the issue, we propose an acousto-optic scanning with spatial-switching multispots (AOSS) method. Inertia-free acousto-optic scanning and nonlinear swept techniques have been developed for achieving ultrahigh-speed and aberration-free scanning. Moreover, a spatial optical switch concept has been implemented to significantly boost the lithography throughput while maintaining high resolution and high design freedom. An eight-foci AOSS system has demonstrated a record-high 3D printing rate of  $7.6 \times 10^7$  voxel  $s^{-1}$ , which is nearly one order of magnitude higher than earlier scanning MPL, exhibiting its promise for future scalable 3D nanomanufacturing.

Supplementary material for this article is available [online](#)

Keywords: 3D nano-printing, acousto-optic scanning, aberration-free wavefront, spatial-switching

## 1. Introduction

In recent years, 3D printing has gained widespread attention owing to its capacity to manufacture complex geometries for end-use components [1–12]. Multiphoton lithography (MPL),

a 3D printing method with a voxel size ranging from sub-micrometer to nanometer, has been widely used in micro-optics [13–17], photonic crystals [18–20], microfluidics [21, 22], meta-surface [23], and mechanical metamaterials [24, 25], which has been regarded as one of the most promising 3D nanomanufacturing technologies.

At present, there are two primary methods for achieving MPL: projection MPL and scanning MPL. The projection MPL can achieve high throughput and sub-micrometer resolution [26] in complex structures [27] using projection-based layers. However, the projection MPL raises demanding requirements for highly sensitive photoresists and

\* Authors to whom any correspondence should be addressed.



Original content from this work may be used under the terms of the [Creative Commons Attribution 4.0 licence](#). Any further distribution of this work must maintain attribution to the author(s) and the title of the work, journal citation and DOI.

ultra-short pulse duration femtosecond lasers with high power. Furthermore, it is difficult to achieve uniform spatial energy distribution, which leads to a size-dependent thresholding behavior [26] and becomes a barrier to forming arbitrary complex 3D structures. Compared with the projection method, the scanning MPL has intrinsic advantages in producing accurate depth-resolved structures owing to its superior energy distribution uniformity [28] and much broader material applicability [29, 30] because of the higher energy density of focusing spots, which eliminates the need for amplified femtosecond laser and ultralow threshold photoresist. Moreover, the sequential movement of the laser focus in space allows multimaterial 3D self-assembly [31–35], which is beneficial for functional device fabrication. However, serial scanning MPL is unfortunately too slow to be a valuable solution for many practical applications. Although attempts at multi-foci parallelization increase the printing throughput of the scanning MPL, the printing speed is still limited by the inertia of the scanning mirrors [36–39], and it can only print periodic structures [28, 40–44], resulting in a loss of nanomanufacturing flexibility. Therefore, it remains a serious challenge to take advantage of both scanning and projection methods while avoiding their shortcomings to achieve arbitrary complex 3D structures with high throughput, high accuracy, and broad material applicability.

In this study, we propose a new MPL method of acousto-optic scanning with spatial-switching multispots (AOSS) that combine the merits of both scanning and projection MPL methods. We used acousto-optic scanning instead of inertial mechanical scanning to drastically increase the laser scanning speed. While to overcome the accompanying spatiotemporal light dispersion and aberration issues introduced by the acousto-optic deflector (AOD), a Kepler dispersion compensation module and a cylindrical lens were designed. And most importantly, a nonlinear signal modulation technique of the AOD was accomplished to ensure that the spot size met the diffraction limit during the high-speed acousto-optic scanning. Furthermore, to improve resolution, we used a digital mask that functions as a spatial optical switch to activate and deactivate beams with different scanning angles. Whether the beam was allowed to pass was independent of the moment it reached the specified angle. Therefore, the resolution was not limited by the frequency of temporal optical switching as usual. The resolution along the scanning direction reaches 220 nm, which meets the accuracy requirements determined by the voxel size (212 nm in this work). With the small voxel size of aberration-free acousto-optic scanning and the high resolution of the spatial optical switch, a milestone of  $9.5 \times 10^6$  voxel  $s^{-1}$  for a single-focus 3D printing has been achieved. Furthermore, since the spatial optical switch controls the multi-foci switching individually, every focus can print a different structure independently and simultaneously. On this premise, a higher throughput was achieved through parallel scanning. We demonstrated an eight-foci MPL system with a printing rate of  $7.6 \times 10^7$  voxel  $s^{-1}$ , which is nearly an order of magnitude higher than the best track record of the state-of-the-art galvanometer-based MPL [28], with enhanced spatial resolution and design freedom. The AOSS

printing rate is comparable to the projection-based method and possesses great potential to achieve higher throughput and a wider range of material applicability. It is anticipated that the proposed AOSS with high throughput, high resolution, wide material adaptability, and design flexibility will be a practical technology for nanomanufacturing wafer-scale functional components with complex 3D micro and nanostructures, such as metamaterials, micro-optics, micromechanical devices, and tissue engineering scaffolds.

## 2. Results

The optical diagram of our AOSS method is presented in figure 1(a), which mainly contains two modules: an inertial-free AO scanning module and a multi-split spatial optical switch module. The inertial-free AO scanning module containing a two-axis AOD (including an AOD<sub>x</sub> and an AOD<sub>y</sub>) deflects the femtosecond laser without mechanical rotation. The AOD<sub>x</sub> points the laser to the beginning of each line. The AOD<sub>y</sub> enables continuous scanning with a speed of  $2.091 \text{ m s}^{-1}$ . The deflected beams have an aberration-free wavefront due to a non-linear swept signal being used to drive the AOD<sub>y</sub>. When the AOD<sub>y</sub> is driven by a non-linear signal, the wavefront of the deflected laser is significantly different from the linear swept signal which was widely used in the past [45–48]. The comparison of the wavefront while AOD<sub>y</sub> is driven by ‘non-linear swept’ and the ‘linear swept’ is shown in figure 1(b). The ‘non-linear swept’ wavefront meets the strict standards of diffraction-limited, which means the root mean square (RMS) value of a wavefront is below  $0.05\lambda$  [49]. In contrast, the RMS value of the ‘linear swept’ wavefront in the edge of the scanning angle does not meet the diffraction-limited requirements and is 2.76 times larger than the ‘non-linear swept’ one (58.6 nm versus 21.2 nm). The peak-to-valley (PV) value of the above two wavefronts is 298 nm and 118 nm, respectively. Both RMS and PV values indicate that non-linear swept acousto-optic scanning has better wavefront quality than linear swept acousto-optic scanning.

The multi-split spatial optical switch module consists of three components: a diffractive optical element (DOE), a first tube lens (TL1), and a digital mask. The scanning laser is split into multi beams by the DOE. The splitting beams are then collected by the TL1 on the digital mask. We use a digital micromirror device (DMD) to be the digital mask with high frame refresh rates of up to 22.7 kHz [50]. The digital mask is located on the back focal plane of TL1. Laser beams with different scanning angles are focused on the different areas of the surface of the digital mask. The digital mask controls the optical switch of the laser beams by switching each pixel. Whether the beam was allowed to pass or not was independent of the moment it reached the specified angle. Thus, the resolution is not limited by the frequency of temporal optical switching. In addition, the digital mask is divided into multi parts to control the switch of multi-foci separately. Therefore, the pattern of the switching scanning laser will not have to be as periodic as the arrangement of multi beams.

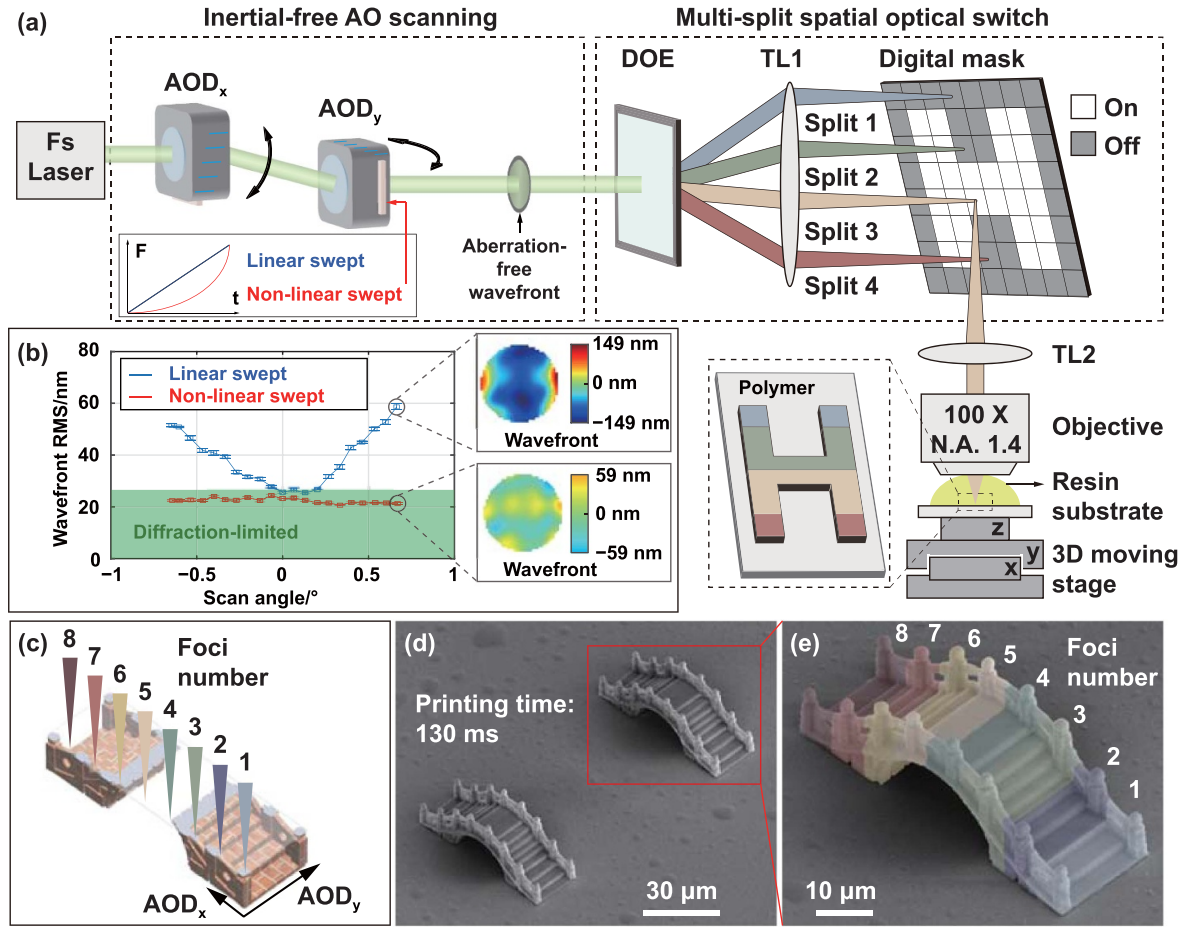


**Figure 1.** Acousto-optic scanning multiphoton lithography based on spatial optical switch. (a) The schematic of the AOSS. The laser beam is deflected by inertial-free acousto-optic scanning. The wavefront of deflected laser is aberration-free due to the AOD<sub>y</sub> being driven by a non-linear swept signal. Then the laser is switched by a multi-split spatial optical switch, which contains a DOE to split the laser into multi-beams and a digital mask to switch beams individually with different areas adjacent to each other. The switched beams are tightly focused by a high N.A. objective and selectively exposure the resin to produce the patterned polymer. The pattern is displayed on the digital mask. (b) The comparison of the wavefront while the AOD<sub>y</sub> is driven by a linear swept signal and a non-linear swept signal, respectively. (c) The schematic of the printing process of a stone bridge printed by eight-foci AOSS. (d) The SEM image of the printed bridge. The bridge is printed in 130 ms. (e) The color processing area of the SEM image in (d). Different colored areas represent the independent scanning area of 8 focal points. The scanning ranges of each focal spot are connected to form a whole volume.

The switching 'on' multi beams are collimated by a second tube lens (TL2) and are tightly focused by a high N.A. objective. The multi-foci selectively exposed the resin to produce a patterned polymer. The pattern of the exposed area is determined by the pattern displayed on the digital mask. Complex 3D structures are manufactured with a moving stage shifting along the direction perpendicular to the scan plane (Z-axis direction). The shift along the Z axis is continuous, which aims to save the position time between every two exposed layers [27]. A stone bridge sculpture is manufactured by eight-foci AOSS to demonstrate the above manufacturing methods. The diagram of the eight-foci parallel manufacturing is shown in figure 1(c). Eight-foci scan along the direction of the AOD<sub>x</sub> and AOD<sub>y</sub>. The 8 foci distribute in a straight line which is orthogonal to the scanning direction of the AOD<sub>y</sub>. The scanning range of each focus spot is adjacent to form a connected layer. Each layer has an exposure time of 805 μs. The scanning electron microscope (SEM) images of the printed bridge

are shown in figures 1(d) and (e). The width, length, and height of the bridge are 22 μm, 68 μm, and 27 μm, respectively. The moving speed of the stage along the Z axis is 207 μm s<sup>-1</sup>. The height of each two printing layers is 167 nm. One bridge is printed in 130 ms. It can be estimated that the volumetric yield is 3.1 × 10<sup>2</sup> μm<sup>3</sup> ms<sup>-1</sup>, which is equivalent to printing complex three-dimensional structures larger than the volume of one red blood cell (diameter: 8 μm) in 1 ms. A larger volumetric yield raising with the higher moving speed of the stage will be shown in figure 3.

The conception of the resolution and voxel size of AOSS has presented in figure 2. The resolution is the distance between two resolvable voxels. In this paper, we pay more attention to the resolution along the scanning direction, which is shown in figure 2(a). We manufactured a grating with a cycle of 420 nm. The width of the protruding part of the grating was 220 nm, which is shown in figure 2(b) and demonstrates the best resolution the spatial optical switch could achieve



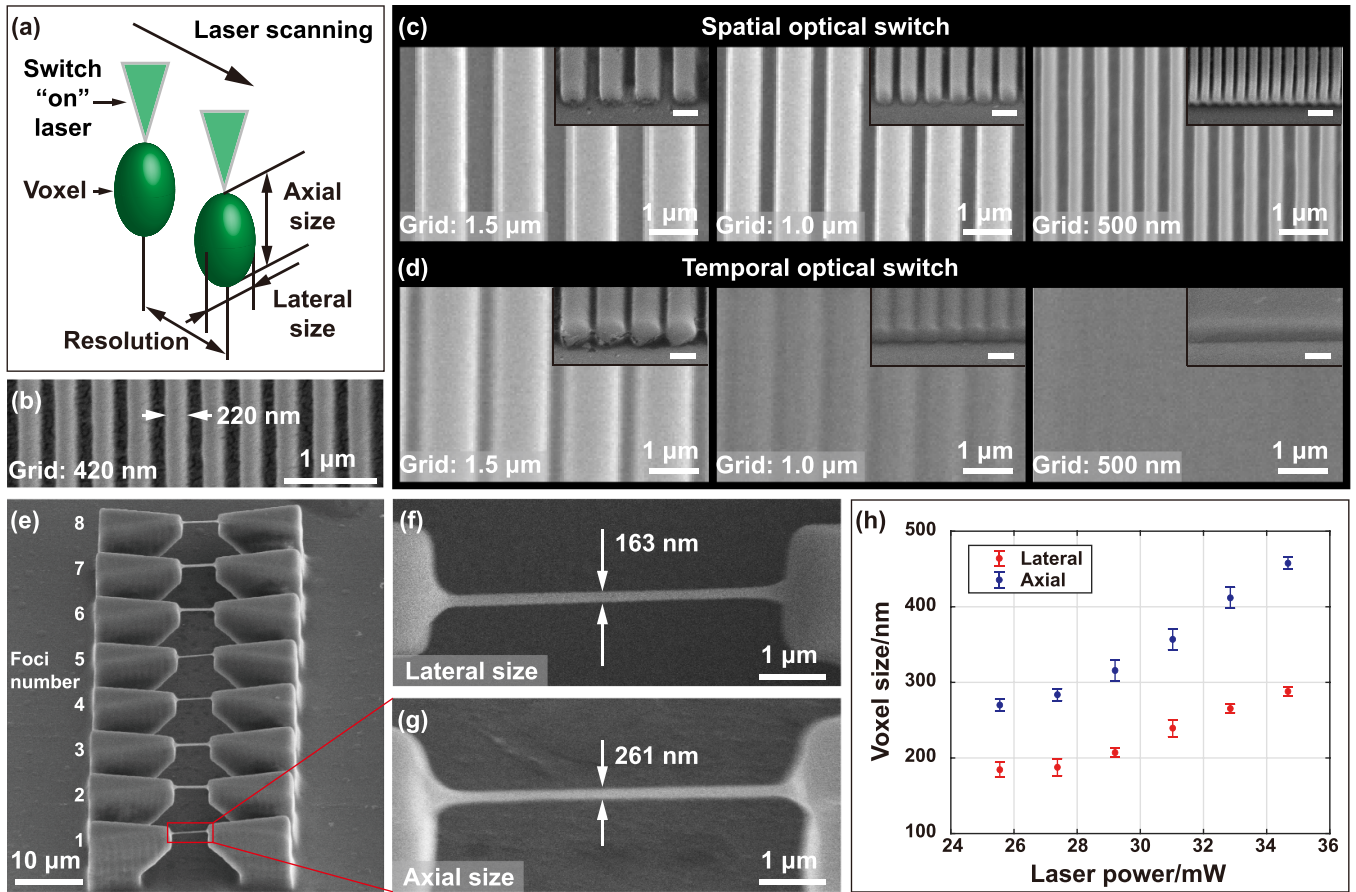


**Figure 2.** The characterization of the resolution and voxel size of AOSS. (a) The resolution between two adjacent voxels. The voxel size is the average of the axial and lateral sizes of a voxel. (b) A grid has a cycle of 420 nm and a protrusion width of 220 nm. (c) Three grids with a cycle of 1.5, 1.0, and 0.5  $\mu\text{m}$  which are printed by the spatial optical switch. (d) Three grids with the same cycles are printed by the temporal optical switch method. The inset SEM image in the upper right corner of (b) and (c) is a 45° side view of the grid. The white scale bar in (c) and (d) is 1  $\mu\text{m}$ . (e) Eight wires between two piers were printed by the eight-foci AOSS. The voxel size of the thinnest wire is 212 nm. (f) The lateral size of the thinnest wire. (g) The axial size of the thinnest wire. The tilted angle of (e)–(g) is 45°. (h) The relationship between voxel size and laser power. The power varies from 25.5 to 34.7 mW. The voxel size varies from 228 to 373 nm. The error bar is one plus/minus the standard deviation of three measurements.

under our experimental conditions. In addition, we compare the advantages of the spatial optical switch method over the temporal optical switch method. Three gratings with cycles of 1.5  $\mu\text{m}$ , 1.0  $\mu\text{m}$ , and 0.5  $\mu\text{m}$  are printed by the spatial optical switch, which is shown in figure 2(c). Contrarily, the gratings with the same cycle are printed by the temporal optical switch, which is shown in figure 2(d). Even with the help of the nonlinearity of the polymerization, only a grating with a cycle of 1.5  $\mu\text{m}$  could be roughly resolved. These comparisons show the resolution of the spatial optical switch has at least three times higher than that of the temporal optical switch at a scanning speed of 2.091  $\text{m s}^{-1}$ . The temporal optical switch used in the comparison is an acousto-optic modulator (AOM) with a switching frequency of 2 MHz, which is similar to the switching frequency of AOM [28] and electro-optic modulator [51] used in previous MPL methods (1 MHz in paper [28] and 3 MHz in paper [51]).

As for the minimum voxel size that can be gotten by eight-foci AOSS, we measure the size of eight hanging lines manufactured by eight foci, which is shown in figure 2(e). The

thinnest line is manufactured by focus 1. The lateral size of the thinnest wire is 163 nm, which is shown in figure 2(f). The axial size is gotten by the measured height of the 45° tilted SEM images of the line multiplied  $\sqrt{2}$ . Thus, the axial size is  $184 \times \sqrt{2} = 261$  nm, which is shown in figure 2(g). Therefore, the voxel size is 212 nm by averaging the lateral and axial sizes. The total laser power of eight-foci in figures 2(e)–(g) is 260 mW. By controlling the power, we can adjust the voxel size range from 228 to 373 nm to meet different printing speeds. The axial size of a voxel can be adjusted from 270 nm to 458 nm. With the help of the optical proximity effect [52], we can achieve a printing layer height of 500 nm or a printing speed of 621  $\mu\text{m s}^{-1}$  along the Z-axis. The relationship between voxel size and laser power is shown in figure 2(h).

Various 3D models, arrays, and multi-level structures are printed to show the printing accuracy and yield of our AOSS method. Three printed soccer, a hollow nanolattice [53], and a metamaterial are printed by single-focus AOSS, which is shown in figures 3(a)–(c). The smallest printed soccer has a diameter of 8.5  $\mu\text{m}$ , which is close to the size of the previously

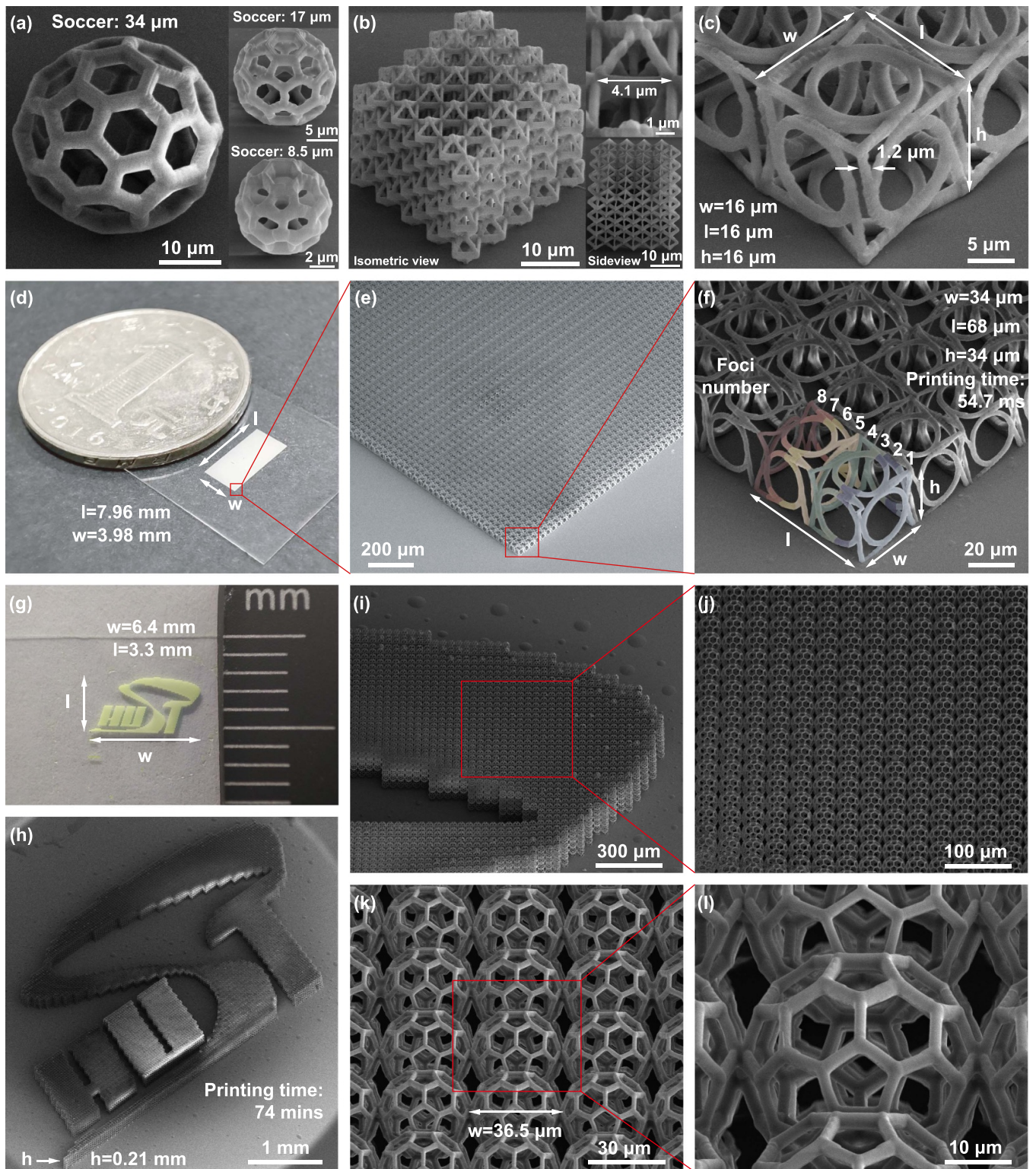


**Figure 3.** The 3D models which are printed by AOSS. (a) Three soccer balls with the following diameters: 34, 17, and 8.5  $\mu\text{m}$ . The printing times for (a) are 436, 218, and 269 ms, respectively. (b) A hollow nanolattice [53] has a width of 34  $\mu\text{m}$  and a height of 30.5  $\mu\text{m}$ . Each unit has a width of 4.1  $\mu\text{m}$ . (c) A metamaterial unit that has a side length of 16  $\mu\text{m}$  and an arbitrary frame with a width of 1.2  $\mu\text{m}$ . The printing times of (b) and (c) are 393 and 64.5 ms, respectively. (d) An array of metamaterials placed next to a coin. The array is printed by using eight-foci AOSS. (e) The enlarged SEM image of (d). (f) The unit of the array in (d). The scanning times of (d) and (f) are 12.5 min and 54.7 ms, respectively. (g)–(h) A multi-level structure, a ‘HUST’ logo printed by our AOSS method. (i)–(k) The multi-scale enlarged SEM image of (h). (l) The unit of the logo in (g) and (h). The ‘HUST’ logo in (g) and (h) consists of 44 844 units shown in (l). The designed spaces between two adjacent soccer are 36.5, 34, and 35.0  $\mu\text{m}$ , respectively. The printing time of the logo in (g) and (h) is 74 min.



reported ‘nano bull’ [54]. The printed hollow nanolattice has a period of  $4.1 \mu\text{m}$  and submicron line width. The printed metamaterial unit has a side length of  $16 \mu\text{m}$  and  $1 \mu\text{m}$ -level details in arbitrary directions, which is similar to the previous results printed by the two-step absorption 3D nano-printing method [7]. We use a commercial printing system (Nanoscribe Professional GT2) to manufacture the same unit shown in figure 3(c) to compare the printing time of single-focus AOSS with the leading commercial printing system. The commercial printing system uses a galvanometer to scan the laser. The results printed by the commercial printing system are shown in figures S1(a), (b), and text S1. The printing time of one  $16 \mu\text{m}$  unit is 4.38 s at the maximum scanning speed ( $100 \text{ mm s}^{-1}$ ) and the maximum acceleration ( $10 \text{ V } \mu\text{s}^{-2}$ ). The above comparison indicates that the printing speed of acousto-optic scanning MPL is 67 times higher than that of the traditional galvanometer-based MPL method.

We print an array of a metamaterial by eight-foci AOSS to show the capability of high-throughput parallel printing. The array is placed next to a coin, as shown in figure 3(d). The length and width of this structure were 7.95 and 3.98 mm, respectively. The array contained  $234 \times 117$  units. The unit details are shown in figures 3(e) and (f). Each unit has a width, length, and height of  $34 \mu\text{m}$ ,  $68 \mu\text{m}$ , and  $34 \mu\text{m}$ , respectively. The printing time of one unit as shown in figure 3(f) is 54.7 ms. Therefore, the peak volumetric yield is  $1.52 \times 10^3 \mu\text{m}^3 \text{ ms}^{-1}$ , which is more than 10 times higher than that of the single-focus AOSS ( $9.0 \times 10^1 \mu\text{m}^3 \text{ ms}^{-1}$  in figure 3(b)). We also use a commercial printing system to manufacture the unit as shown in figure 3(f) to compare the printing speed of eight-foci AOSS with the commercial printing system. The results printed by the commercial printing system are shown in figures S1(c), (d), and text S1. The printing time of the commercial printing system is 27 s under the same conditions as above. The above comparison shows that eight-foci AOSS is 490 times faster than the commercial scanning MPL system.

We print a ‘HUST’ logo to show the capability of printing multi-level structures by the eight-foci AOSS method. The width, length, and height of the logo are 6.4 mm, 3.3 mm, and 0.21 mm, respectively, which is shown in figures 3(g) and (h). The soccer structure is the secondary structure of the logo. The width of the soccer unit cell is  $36.5 \mu\text{m}$ , which reaches the maximum scanning range. An overlap between two soccer along the width direction is set to  $0.5 \mu\text{m}$  to ensure a secure connection. We print 44 844 soccer to make up the logo in 74 min. The details of the soccer are shown in figures 3(g)–(l). The block printing speed is 10.1 blocks per second considering the smallest repeating units as a printing ‘block’ [28]. The block in figures 3(g)–(l) is soccer. In previous reports, the two fastest block printing speeds are 1.67 blocks per second [28] and 8.95 blocks per second [27]. The block printing speed of eight-foci AOSS is the fastest as we know.

We compare the AOSS method with other methods in terms of voxel size and voxel printing rate. The voxel printing rate can be characterized by the quotient of the acousto-optic scanning speed and the resolution. Our AOSS method has a voxel size of 212 nm and a resolution of 220 nm. The scanning speed of our acousto-optic scanning method is  $2.091 \text{ m s}^{-1}$ .

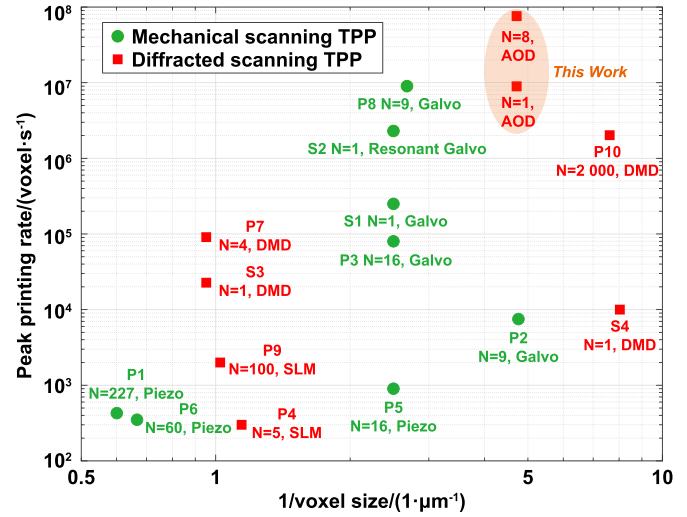


**Figure 4.** The comparison of the voxel printing rate of scanning MPL methods. The horizontal axis shows inverse voxel size, ranging from  $0.5 \mu\text{m}^{-1}$  to  $10 \mu\text{m}^{-1}$  (voxel size ranges from  $2 \mu\text{m}$  to  $100 \text{ nm}$ ). The vertical axis represents the voxel printing rate, ranging from  $1 \times 10^2$  to  $1 \times 10^8 \text{ voxel s}^{-1}$ . The number of focal spots used in this study is represented by the legend ‘N’. The legends ‘Piezo’, ‘Galvo’, and ‘Resonant Galvo’ represent the scanners for mechanical TPP scanning. The legends ‘DMD’ and ‘SLM’ represent the scanners for diffracted TPP scanning. S1 [55], S2 [51], S3 [50], and S4 [59] are single-focus scanning MPLs. P1 [40], P2 [41], P3 [56], P4 [57], P5 [42], P6 [44], P7 [50], P8 [28], P9 [58] and P10 [60] are the multi-foci scanning MPLs. The serial number after ‘S’ and ‘P’ shows the publication year in chronological order.

Therefore, the voxel printing rate of single-focus AOSS is  $9.5 \times 10^6 \text{ voxel s}^{-1}$ . The voxel printing rate of eight-foci AOSS reaches  $7.6 \times 10^7 \text{ voxel s}^{-1}$ . The comparison of our work and the reported scanning MPL methods is presented in figure 4.

On the one hand, we compare our work with the reported mechanical scanning MPL methods. Initially, a piezo stage is used to scan laser spots in the resin [40, 42, 44], and the printing rate does not exceed  $1 \times 10^2 \text{ voxel s}^{-1}$ . Subsequently, the printing rate increases from  $1 \times 10^3$  to  $1 \times 10^6 \text{ voxel s}^{-1}$  while a galvanometer is used to deflect the beam [41, 55, 56]. In 2019, resonant scanning significantly increases the printing rate to  $2.3 \times 10^6 \text{ voxel s}^{-1}$  [51]. At the same time, mechanical scanning MPL methods increase throughput by incorporating multi-foci parallel manufacturing [28, 40–42, 44, 56]. In 2020, a nine-foci scanning MPL method with a high-performance galvanometer records the best printing rate of  $9 \times 10^6 \text{ voxel s}^{-1}$  [28]. The voxel printing rate of our AOSS method is 8.4 times more than the record of the mechanical scanning MPL method. The parameters of the above comparison are shown in table S1.

On the other hand, we compare our work with the reported diffracted scanning MPL. A spatial light modulator (SLM) [57, 58], and a DMD [50, 59] are used to realize multi-foci scanning by refreshing the holograms frame by frame and positioning the laser spots point by point. The higher refresh rate of the device enables a higher printing rate. Four-foci scanning with a single-focus printing rate of  $2.27 \times 10^4 \text{ voxel s}^{-1}$  and

multi-foci printing rate of  $9.08 \times 10^4$  voxel  $s^{-1}$  is reported in 2019 [50]. About 2000-foci parallel manufacturing with a printing rate of  $2.0 \times 10^6$  voxel  $s^{-1}$  is reported in 2023 [60], which is the highest diffracted scanning MPL method recorded to date. Due to the continuous movement of laser spots in AOSS, the voxel printing rate of AOSS is up to 37 times more than the record of the diffracted scanning MPL method. The parameters of the above comparison are shown in table S2.

### 3. Discussion

In this study, we present an AOSS method to significantly improve the MPL scanning throughput while maintaining high printing resolution and flexibility. In the future, a higher acousto-optic scanning speed and an increased number of foci can continue to increase the throughput of AOSS. The scanning speed of acousto-optic scanning is proportional to the bandwidth of the acousto-optic scanning [61]. A step-array AOD based on  $PbMoO_4$  had a 3 dB bandwidth of 250 MHz [62], which is 4.5 times wider than the 55.7 MHz bandwidth of our current work. Besides, the AOD based on  $LiNbO_3$  demonstrates the 3 dB bandwidth of 1 GHz [63]. Therefore, the scanning speed has the potential to improve by one order of magnitude using a wider bandwidth. As for increasing the foci number, higher laser power can support more laser spots. To address the energy requirements of eight-foci, we used a laser source with a power of merely 6.5 W. As the average power of femtosecond lasers increases from 100 to 10000 W [64–66], the number of laser spots can further expand to hundreds or even tens of thousands. Based on the above analysis, the throughput of AOSS has a foreseeable potential to increase by three orders of magnitude without sacrificing the structural design freedom, uniformity of parallel processing, and accuracy, which will create new possibilities and pave the way toward massive industrialized MPL 3D nano-printing.

### 4. Materials and methods

#### 4.1. The optical structure of our AOSS method

The detailed diagram of the AOSS is shown in figure S2. The laser is a femtosecond laser (Keyun, China, 250 fs pulse width, 45 MHz repetition rate, 6.5 W). A pair of prisms, P1 and P2 (Thorlabs, N-F2, USA), is used to pre-compensate the group delay dispersion of the system. An AOM (Gooch, AOMO 3080-294, UK) controls the temporal optical switch of the system. The switching frequency of AOM can be calculated from the aperture and sound velocity [67]. The aperture of the beam passing through the AOM is 2 mm, and the sound velocity of the AOM is  $5730 \text{ m s}^{-1}$ . From this, it is calculated that the rise time is 230 ns, and the 3 dB switching frequency is 2 MHz.

A prism, P3 (Thorlabs, N-F2, USA), is used to offer pre-compensation for the angular dispersion of the AOD on the center of the field. A two-axis AOD (AA Opto-Electronic, DTSXY400, France) deflects the femtosecond laser at different angles. The  $AOD_x$  and  $AOD_y$  are driven by a pair of RF generators (AA Opto-Electronic, DRFA10Y-B, France) and a pair of power amplifiers (AA Opto-Electronic, AMPB-B-34,

France). The RF generators are controlled by an arbitrary waveform generator (NI Instruments, pixie-5413, USA). A DOE (Lubang, China) splits the beam into eight beamlets. The direction of beam division is perpendicular to the fast axis ( $AOD_y$ ). The beam is nearly vertical incident DOE. The angle between the incident beam and the normal direction of the DOE is  $\pm 0.14^\circ$  and  $\pm 0.7^\circ$  along the scanning direction of  $AOD_x$  and  $AOD_y$ , respectively.

The uniformity of the eight-foci is mainly affected by the DOE. We measured the voxel size and intensity of each focus, which is shown in figure 2(e). The optical power of each focus is shown in figure S3(a). The uniformity of our DOE is calculated by the following formula [68]:

$$u = 1 - \frac{P_{\max} - P_{\min}}{P_{\max} + P_{\min}} \quad (1)$$

$P_{\max}$  and  $P_{\min}$  are the maximum and minimum values of the optical power of eight-foci, respectively, and the uniformity of DOE is 0.881. There is an approximate linear relationship between the voxel size and the optical power of each focus, which is shown in figure S3(b). The lateral size and axial size of each focus are shown in figures S3(c) and (d).

The scanning range of  $AOD_x$  and  $AOD_y$  is  $68 \mu\text{m}$  and  $36.6 \mu\text{m}$ , respectively, which is shown in figure S4. The pitch of each of the eight-foci is  $8.5 \mu\text{m}$ .  $AOD_x$  scans 46 points at a hatching distance of 185 nm to form a layer. The scanning period of  $AOD_y$  is  $17.5 \mu\text{s}$ . Therefore, the processing time of each layer is  $805 \mu\text{s}$ .

Angular dispersion occurs when the femtosecond laser passed through the AOD and DOE. A Kepler dispersion telescope (KDCM) can compensate for the angular dispersion generated by the AOD [69] and DOE [28], respectively. In this study, the DOE is placed close to the exit pupil of  $AOD_y$ . A custom-designed KDCM compensates for the angular dispersion generated by the AOD and DOE. The results of compensation are shown in figure S5 and text S2. A cylindrical lens (CL1, Thorlabs, LJ1277L1-A, USA) with a 250 mm focal length compensates for the cylindrical lens effect caused by  $AOD_y$ . A tube lens, TL1 (Olympus, SWTLU-C, Japan), collects the above eight laser beams onto the surface of a digital mask (TI, DLP6500, USA).

The digital mask is located on the back focal plane of TL1. CL1 is on the front focal plane of TL1. The digital mask has a blaze angle of  $12^\circ$ . The incident angle  $\theta_{i,\text{mask}}$ , and outgoing angle  $\theta_{o,\text{mask}}$  of the digital mask meets the 2D blazed grating diffraction theory [70]

$$(\sin(\theta_{o,\text{mask}}) - \sin(\theta_{i,\text{mask}})) \times \frac{d}{\sqrt{2}} = m \times \lambda. \quad (2)$$

In this study, we use  $\theta_{i,\text{mask}} = 10^\circ$ ,  $\theta_{o,\text{mask}} = 34^\circ$ ,  $m = 4$  for a 517 nm laser. The parameter  $d$  in formula (2) is the pixel size of the digital mask, and  $d = 7.56 \mu\text{m}$ .

The laser beams are then relayed by another tube lens, TL2 (Olympus, SWTLU-C, Japan), tightly focused by a high NA lens (Olympus, 100 X, NA 1.4, Japan). A moving stage (AUS-PRECISION, QFL100-100XY-15V, China) is used to position the scanning region.



#### 4.2. The measurement of the wavefront of acousto-optic scanning

We develop an optical measurement system to measure the wavefront of acousto-optic scanning. The diagram of the measurement system is presented in figure S6. To extract the beam at a specific scanning angle of the acousto-optic scanning, we use a bi-convex lens (f1, LB1391-A, Thorlabs, USA) to focus the single longitudinal mode laser (ZK Laser, SLM532G-200, Beijing, China) into the AOM (Gooch, AOMO 3080-294, UK) to reduce the rise time to 25 ns. A pinhole with a diameter of 50  $\mu\text{m}$  and a collimating lens (f2, LA1172-A, Thorlabs, USA) is used to generate a planar wave with a wavefront RMS value of 11 nm. We use a cylindrical lens (f3, LJ1277L1-A, Thorlabs, USA) with a focal length of 250 mm to compensate for the cylindrical lens effect caused by acousto-optic scanning. A pair of tube lenses (f4 and f5, SWTLU-C, Olympus, Japan) is used to relay the beam on the surface of the wavefront sensor (WFS30-5C, Thorlabs, USA). An aperture (GCM-5702M, Daheng Optics, Beijing, China) is located at the confocal plane of the relay, which aims to allow only the wavefront of the first order of diffracted light to be measured. The wavefront of 21 locations in the scanning field is measured.

The eight wavefronts of the measurement result in figure 1(b) are shown in figure S7(a). The wavefront of the acousto-optic scanning driven by linear swept signal has significant aberrations at the scanning edges. By analyzing the Zernike coefficient of the measuring wavefronts, we find that the variation of the focal power of the cylindrical lens effect is the main source of the aberrations. The focal power of the cylindrical lens effect ( $\phi$ ) can be expressed by the 90° astigmatism coefficient, which is recorded as  $Z_2^{+2}$

$$\phi = \frac{4\sqrt{6}\lambda}{r^2} \times Z_2^{+2}. \quad (3)$$

The  $r$  in formula (3) is the radius of the measured aperture of the wavefront sensor.  $r = 2.55$  mm is used in this measurement.

#### 4.3. The non-linear swept acousto-optic scanning method

The focal power calculated by the formula (3) is shown in figure S7(b). As for acousto-optic scanning driven by linear swept signal, the calculated focal power ranges from  $-0.052 \text{ m}^{-1}$  to  $+0.068 \text{ m}^{-1}$ , of which the variation is 3% relative to the focal power of lens f3. We use a non-linear swept signal to achieve a nearly constant cylindrical lens effect. The nearly constant cylindrical lens effect is shown in figure S7(b). The calculated focal power ranges from  $-0.004 \text{ m}^{-1}$  to  $+0.014 \text{ m}^{-1}$ , of which the variation is only 0.45% relative to the focal power of lens f3. Based on this, the non-linear swept acousto-optic scanning method also greatly reduces wavefront aberration, which is shown in figures 1(b) and S7(a). The non-linear swept signal is

$$F(t) = \sum_{i=0}^n a_i \times \left(\frac{t}{T}\right)^i. \quad (4)$$

$T$  in formula (4) is the scanning period of AOD<sub>y</sub>. We do not stop adjusting the second-order coefficient  $a_2$  until the measured focal power of the cylindrical lens effect is nearly constant. Higher-order coefficients ( $i \geq 3$ ) may be used for performing faster acousto-optic scanning in the future.

#### 4.4. Printing processing and structure characterization

The resin used in this study is IP-L and IP-Dip (Nanoscribe, Germany). The post-print processing for the sample included a propylene glycol monomethyl ether acetate (PGMEA) bath for 10 min and another IPA bath for 5 min. The sample dries at a room temperature of 24 °C. The sample coated with Au is imaged using a field emission scanning electron microscope (FEI Nova NanoSEM450) at 5–10 kV. The microscope images are obtained by using 3D laser scanning confocal microscope (LSCM, Keyence VK-X1100).

#### 4.5. Module processing

The slicing distance and hatching distance of the printed models are shown in table S3.

### Data and materials availability

All data are available in the main text or the supplementary materials.

### Acknowledgments

The authors thank the technical support of the Analytical and Testing Center of HUST, the Optoelectronic Micro&Nano Fabrication and Characterizing Facility at Wuhan National Laboratory for Optoelectronics of HUST, and the Experiment Center for Advanced Manufacturing and Technology in the School of Mechanical Science and Engineering of HUST. The authors also thank the primary editor Leandra C of Enago for the English grammar modification and polishing.

### Funding

National Key Research and Development Program of China (2021YFF0502700)

National Natural Science Foundation of China (52275429, 62205117)

Innovation project of Optics Valley Laboratory (OVL2021ZD002)

Hubei Provincial Natural Science Foundation of China (2022CFB792)

Young Elite Scientists Sponsorship Program by CAST (2022QNRC001)

West Light Foundation of the Chinese Academy of Sciences (xbzg-zdsys-202206)

Knowledge Innovation Program of Wuhan-Shuguang

## Author contributions

Conceptualization: B J, W X, H G.  
 Methodology: B J, F C.  
 Investigation: B J, F C, X F, Y L, Q D.  
 Visualization: B J, H G.  
 Supervision: W X, H G.  
 Writing—original draft: B J, H G.  
 Writing—review & editing: W X, B J, H G, S Z.

## Conflict of interest

B J, H G, Y L, X F, L D, and W X are inventors of two patents application related to this work filed by Huazhong University of Science and Technology (No. US 2022/0221796 A1, filed 14 October 2021, and No. ZL 202110045996.8, filed 14 January 2021). The authors declare they have no other competing interests.

## ORCID iDs

Binzhang Jiao  <https://orcid.org/0000-0002-5083-3938>  
 Xuhao Fan  <https://orcid.org/0000-0002-6148-0883>  
 Hui Gao  <https://orcid.org/0000-0002-2155-4681>  
 Wei Xiong  <https://orcid.org/0000-0002-2532-2503>

## References

- [1] Kelly B E, Bhattacharya I, Heidari H, Shusteff M, Spadaccini C M and Taylor H K 2019 Volumetric additive manufacturing via tomographic reconstruction *Science* **363** 1075–9
- [2] Zheng X Y *et al* 2016 Multiscale metallic metamaterials *Nat. Mater.* **15** 1100–6
- [3] Tumbleston J R *et al* 2015 Continuous liquid interface production of 3D objects *Science* **347** 1349–52
- [4] Walker D A, Hedrick J L and Mirkin C A 2019 Rapid, large-volume, thermally controlled 3D printing using a mobile liquid interface *Science* **366** 360–4
- [5] Regehy M, Garmshausen Y, Reuter M, König N F, Israel E, Kelly D P, Chou C-Y, Koch K, Asfari B and Hecht S 2020 Xolography for linear volumetric 3D printing *Nature* **588** 620–4
- [6] Hahn V, Rietz P, Hermann F, Müller P, Barner-Kowollik C, Schlöder T, Wenzel W, Blasco E and Wegener M 2022 Light-sheet 3D microprinting via two-colour two-step absorption *Nat. Photon.* **16** 784–91
- [7] Hahn V, Messer T, Bojanowski N M, Curticean E R, Wacker I, Schröder R R, Blasco E and Wegener M 2021 Two-step absorption instead of two-photon absorption in 3D nanoprining *Nat. Photon.* **15** 932–8
- [8] Sanders S N, Schloemer T H, Gangishetty M K, Anderson D, Seitz M, Gallegos A O, Stokes R C and Congreve D N 2022 Triplet fusion upconversion nanocapsules for volumetric 3D printing *Nature* **604** 474–8
- [9] Chen Y Q, Shu Z W, Zhang S, Zeng P, Liang H K, Zheng M J and Duan H G 2021 Sub-10 nm fabrication: methods and applications *Int. J. Extrem. Manuf.* **3** 032002
- [10] Ge Q, Li Z Q, Wang Z L, Kowsari K, Zhang W, He X N, Zhou J L and Fang N X 2020 Projection micro stereolithography based 3D printing and its applications *Int. J. Extrem. Manuf.* **2** 022004
- [11] Chen L, Duan G H, Zhang C, Cheng P and Wang Z L 2022 3D printed hydrogel for soft thermo-responsive smart window *Int. J. Extrem. Manuf.* **4** 025302
- [12] Zhang W Q, Ye H T, Feng X B, Zhou W Z, Cao K, Li M Y, Fan S F and Lu Y 2022 Tailoring mechanical properties of P $\mu$ SL 3D-printed structures via size effect *Int. J. Extrem. Manuf.* **4** 045201
- [13] Gissibl T, Thiele S, Herkommer A and Giessen H 2016 Two-photon direct laser writing of ultracompact multi-lens objectives *Nat. Photon.* **10** 554–60
- [14] Porte X, Dinc N U, Moughames J, Panusa G, Juliano C, Kadic M, Moser C, Brunner D and Psaltis D 2021 Direct (3+1)D laser writing of graded-index optical elements *Optica* **8** 1281–7
- [15] Kubec A, Zdora M-C, Sanli U T, Diaz A, Vila-Comamala J and David C 2022 An achromatic x-ray lens *Nat. Commun.* **13** 1305
- [16] Chan J Y E, Ruan Q F, Jiang M H, Wang H T, Wang H, Zhang W, Qiu C-W and Yang J K W 2021 High-resolution light field prints by nanoscale 3D printing *Nat. Commun.* **12** 3728
- [17] Nair S P, Trisno J, Wang H T and Yang J K W 2021 3D printed fiber sockets for plug and play micro-optics *Int. J. Extrem. Manuf.* **3** 015301
- [18] Liu S-F, Hou Z-W, Lin L H, Li F, Zhao Y, Li X-Z, Zhang H, Fang H-H, Li Z C and Sun H-B 2022 3D nanoprining of semiconductor quantum dots by photoexcitation-induced chemical bonding *Science* **377** 1112–6
- [19] Wang H, Ruan Q F, Wang H T, Rezaei S D, Lim K T P, Liu H L, Zhang W, Trisno J, Chan J Y E and Yang J K W 2021 Full color and grayscale painting with 3D printed low-index nanopillars *Nano Lett.* **21** 4721–9
- [20] Zhang W *et al* 2021 Structural multi-colour invisible inks with submicron 4D printing of shape memory polymers *Nat. Commun.* **12** 112
- [21] Nielson R, Kaehr B and Shear J B 2009 Microreplication and design of biological architectures using dynamic-mask multiphoton lithography *Small* **5** 120–5
- [22] Zhang C C, Zhang J M, Chen R F, Li J W, Wang C W, Cao R, Zhang J J, Ye H C, Zhai H and Sugioka K 2020 Rapid fabrication of high-resolution multi-scale microfluidic devices based on the scanning of patterned femtosecond laser *Opt. Lett.* **45** 3929–32
- [23] Ren H R, Fang X Y, Jang J, Bürger J, Rho J and Maier S A 2020 Complex-amplitude metasurface-based orbital angular momentum holography in momentum space *Nat. Nanotechnol.* **15** 948–55
- [24] Sun L D *et al* 2020 3D-printed cellular tips for tuning fork atomic force microscopy in shear mode *Nat. Commun.* **11** 5732
- [25] Frenzel T, Kadic M and Wegener M 2017 Three-dimensional mechanical metamaterials with a twist *Science* **358** 1072–4
- [26] Saha S K, Wang D, Nguyen V H, Chang Y, Oakdale J S and Chen S-C 2019 Scalable submicrometer additive manufacturing *Science* **366** 105–9
- [27] Somers P, Liang Z H, Johnson J E, Boudouris B W, Pan L and Xu X F 2021 Rapid, continuous projection multi-photon 3D printing enabled by spatiotemporal focusing of femtosecond pulses *Light Sci. Appl.* **10** 199
- [28] Hahn V, Kiefer P, Frenzel T, Qu J Y, Blasco E, Barner-Kowollik C and Wegener M 2020 Rapid assembly of small materials building blocks (voxels) into large functional 3D metamaterials *Adv. Funct. Mater.* **30** 1907795
- [29] Wen X W *et al* 2021 3D-printed silica with nanoscale resolution *Nat. Mater.* **20** 1506–11
- [30] Kotz F, Quick A S, Risch P, Martin T, Hoose T, Thiel M, Helmer D and Rapp B E 2021 Two-photon polymerization of nanocomposites for the fabrication of transparent fused silica glass microstructures *Adv. Mater.* **33** 2006341

- [31] Merkininkaitė G, Aleksandravičius E, Malinauskas M, Gailevičius D and Šakirzanovas S 2022 Laser additive manufacturing of Si/ZrO<sub>2</sub> tunable crystalline phase 3D nanostructures *Opto-Electron. Adv.* **5** 210077
- [32] Liu J W, Liu Y C, Deng C S, Yu K W, Fan X H, Zhang W G, Tao Y F, Hu H C, Deng L M and Xiong W 2022 3D printing nano-architected semiconductors based on versatile and customizable metal-bound composite photoresins *Adv. Mater. Technol.* **7** 2101230
- [33] Fan X H, Deng C S, Gao H, Jiao B Z, Liu Y C, Chen F Y, Deng L M and Xiong W 2022 3D printing of nanowrinkled architectures via laser direct assembly *Sci. Adv.* **8** eabn9942
- [34] Long J et al 2020 Directional assembly of ZnO nanowires via three-dimensional laser direct writing *Nano Lett.* **20** 5159–66
- [35] Zhao Y Y, Ren X L, Zheng M L, Jin F, Liu J, Dong X Z, Zhao Z S and Duan X M 2021 Plasmon-enhanced nanosoldering of silver nanoparticles for high-conductive nanowires electrodes *Opto-Electron. Adv.* **4** 200101
- [36] Brown M K, Gong T J, Neal D R, Roller J P, Luanava S and Urey H 2001 Measurement of the dynamic deformation of a high-frequency scanning mirror using a Shack-Hartmann wavefront sensor *Proc. SPIE* **4451** 480–8
- [37] Brosens P J 1972 Dynamic mirror distortions in optical scanning *Appl. Opt.* **11** 2987–9
- [38] Akondi V, Kowalski B, Burns S A and Dubra A 2020 Dynamic distortion in resonant galvanometric optical scanners *Optica* **7** 1506–13
- [39] Akondi V, Kowalski B and Dubra A 2021 Dynamic wavefront distortion in resonant scanners *Appl. Opt.* **60** 11189–95
- [40] Kato J-I, Takeyasu N, Adachi Y, Sun H-B and Kawata S 2005 Multiple-spot parallel processing for laser micromanufacturing *Appl. Phys. Lett.* **86** 044102
- [41] Dong X-Z, Zhao Z-S and Duan X-M 2007 Micromanufacturing of assembled three-dimensional microstructures by designable multiple beams multiphoton processing *Appl. Phys. Lett.* **91** 124103
- [42] Yan W S, Cumming B P and Gu M 2015 High-throughput fabrication of micrometer-sized compound parabolic mirror arrays by using parallel laser direct-write processing *J. Opt.* **17** 075803
- [43] Zhang Z-Y, Zhang C-C, Hu Y-L, Wang C-W, Li J-W, Su Y-H, Chu J-R and Wu D 2016 Highly uniform parallel microfabrication using a large numerical aperture system *Appl. Phys. Lett.* **109** 021109
- [44] Yang L, El-Tamer A, Hinze U, Li J W, Hu Y L, Huang W H, Chu J R and Chichkov B N 2015 Parallel direct laser writing of micro-optical and photonic structures using spatial light modulator *Opt. Lasers Eng.* **70** 26–32
- [45] Bruening S, Hennig G, Eifel S and Gillner A 2011 Ultrafast scan techniques for 3D- $\mu\text{m}$  structuring of metal surfaces with high repetitive ps-laser pulses *Phys. Proc.* **12** 105–15
- [46] Franz D, Häfner T, Kunz T, Roth G-L, Rung S, Esen C and Hellmann R 2022 Characterization of a hybrid scanning system comprising acousto-optical deflectors and galvanometer scanners *Appl. Phys. B* **128** 55
- [47] Akemann W, Léger J-F, Ventalon C, Mathieu B, Dieudonné S and Bourdieu L 2015 Fast spatial beam shaping by acousto-optic diffraction for 3D non-linear microscopy *Opt. Express* **23** 28191–205
- [48] Katona G, Szalay G, Maák P, Kaszás A, Veress M, Hillier D, Chiovini B, Vizi E S, Roska B and Rózsa B 2012 Fast two-photon *in vivo* imaging with three-dimensional random-access scanning in large tissue volumes *Nat. Met.* **9** 201–8
- [49] Wyant J C and Creath K 1992 *Basic Wavefront Aberration Theory for Optical Metrology (Applied Optics and Optical Engineering Series vol XI)* (New York: Academic)
- [50] Geng Q, Wang D, Chen P F and Chen S-C 2019 Ultrafast multi-focus 3D nano-fabrication based on two-photon polymerization *Nat. Commun.* **10** 2179
- [51] Pearre B W, Michas C, Tsang J-M, Gardner T J and Otchy T M 2019 Fast micron-scale 3D printing with a resonant-scanning two-photon microscope *Addit. Manuf.* **30** 100887
- [52] Arnoux C, Pérez-Covarrubias L A, Khaldi A, Carlier Q, Baldeck P L, Heggarty K, Banyasz A and Monnerau C 2022 Understanding and overcoming proximity effects in multi-spot two-photon direct laser writing *Addit. Manuf.* **49** 102491
- [53] Montemayor L C, Meza L R and Greer J R 2014 Design and fabrication of hollow rigid nanolattices via two-photon lithography *Adv. Eng. Mater.* **16** 184–9
- [54] Kawata S, Sun H-B, Tanaka T and Takada K 2001 Finer features for functional microdevices *Nature* **412** 697–8
- [55] Oakdale J S et al 2017 Direct laser writing of low-density interdigitated foams for plasma drive shaping *Adv. Funct. Mater.* **27** 1702425
- [56] Gittard S D, Nguyen A, Obata K, Koroleva A, Narayan R J and Chichkov B N 2011 Fabrication of microscale medical devices by two-photon polymerization with multiple foci via a spatial light modulator *Biomed. Opt. Express* **2** 3167–78
- [57] Vizsnyiczai G, Kelemen L and Ormos P 2014 Holographic multi-focus 3D two-photon polymerization with real-time calculated holograms *Opt. Express* **22** 24217–23
- [58] Zhang L R et al 2022 Functional shape-morphing microarchitectures fabricated by dynamic holographically shifted femtosecond multifoci *Nano Lett.* **22** 5277–86
- [59] Ren M D, Lu W P, Shao Q, Han F, Ouyang W Q, Zhang T Y, Wang C C L and Chen S C 2021 Aberration-free large-area stitch-free 3D nano-printing based on binary holography *Opt. Express* **29** 44250–63
- [60] Ouyang W Q, Xu X Y, Lu W P, Zhao N, Han F and Chen S-C 2023 Ultrafast 3D nanofabrication via digital holography *Nat. Commun.* **14** 1716
- [61] Dickson L D 1972 Optical considerations for an acoustooptic deflector *Appl. Opt.* **11** 2196–202
- [62] Yao S K and Young E H 1976 Two-hundred (200) MHz bandwidth step-array acousto optic beam deflector *Proc. SPIE* **0090** 23–27
- [63] Kulakov S V, Kludzin V V, Gusev O B, Gabaraev O G, Nefedov V G and Molotok V V 1996 1-GHz bandwidth isotropic acousto-optic cell *Proc. SPIE* **2754** 121–4
- [64] Russbueldt P, Mans T, Rotarius G, Weitenberg J, Hoffmann H D and Poprawe R 2009 400 W Yb: YAG innoslab fs-amplifier *Opt. Express* **17** 12230–45
- [65] Russbueldt P, Mans T, Weitenberg J, Hoffmann H D and Poprawe R 2010 Compact diode-pumped 1.1 kW Yb: YAG innoslab femtosecond amplifier *Opt. Lett.* **35** 4169–71
- [66] Müller M, Aleshire C, Klenke A, Haddad E, Légaré F, Tünnermann A and Limpert J 2020 10.4 kW coherently combined ultrafast fiber laser *Opt. Lett.* **45** 3083–6
- [67] Goutzoulis A P 1994 *Design and Fabrication of Acousto-optic Devices* (New York: CRC Press) (<https://doi.org/10.1201/9781003210221>)
- [68] Chen D H, Gu S Y and Chen S-C 2021 Study of optical modulation based on binary masks with finite pixels *Opt. Lasers Eng.* **142** 106604
- [69] Hu Q, Zhou Z, Lv X and Zeng S 2016 Compensation of spatial dispersion of an acousto-optic deflector with a special Keplerian telescope *Opt. Lett.* **41** 207
- [70] Deng M-J, Zhao Y-Y, Liang Z-X, Chen J-T, Zhang Y and Duan X-M 2022 Maximizing energy utilization in DMD-based projection lithography *Opt. Express* **30** 4692–705